SHADOW-INSENSITIVE MATERIAL DETECTION/CLASSIFICATION WITH ATMOSPHERICALLY CORRECTED HYPERSPECTRAL IMAGERY

Steven M. Adler-Golden[1], Robert Y. Levine[1], Michael W. Matthew[1], Steven C. Richtsmeier[1], Lawrence S. Bernstein[1] John Gruninger[1], Gerald Felde[2], Michael Hoke[2], Gail Anderson[2] and Anthony Ratkowski[2]

1. INTRODUCTION

Hyperspectral imaging (HSI) from airborne or space-based platforms, currently conducted mainly in the 0.4 - 2.5 μm wavelength region, is a valuable technique for detection and classification of materials and objects on the Earth's surface. In a typical analysis, the spectral radiance data are "corrected" or compensated for the atmospheric and illumination conditions to yield spectral reflectance, and the results are processed with any of a variety of algorithms, which may, for example, compare the contents of each pixel with reference spectra for classification, search the scene for a desired material spectrum, or calculate a terrain property such as a vegetation cover index. Atmospheric correction algorithms include several based on first-principles radiation transport models (e.g., Gao *et al*., 1996; Green *et al*., 1996; Richter, 1996; Matthew *et al*., 2000) as well as the Empirical Line Method (ELM), which utilizes known materials in the scene. An alternative approach is to work with the original radiance data; this is effective for identifying scene anomalies and for supervised processing, where the scene elements can be identified visually by an analyst.

Regardless of the analysis method, varying illumination of the ground caused by shadowing or uneven terrain poses problems for detection and classification. The radiance spectra can vary in both shape and amplitude, since the ground-reflected light is altered while the atmospherically scattered components, consisting of backscattering and forward-scattered surface-reflected light ("adjacency" scattering), remain unchanged. To account for the spectral variation, Healey and Slater (1999) developed a simulation-based detection method that involves a 9-dimensional projection spanning combinations of material spectra, atmosphere models, and direct-sun and sky radiance levels. Alternatively, one can work with the spectra output by an atmospheric correction algorithm, which have the atmospheric scattering removed and thus have a much more constant shape. With such processed spectra, a brightness-normalized algorithm such as the Spectral Angle Mapper (SAM) (Kruse *et al*., 1993) can largely compensate for reduced sunlight. However, even the SAM loses effectiveness in shadows, where typically the dominant illumination is from skylight, which is skewed to short (blue-violet) wavelengths. The spectral skewing effect is illustrated in the reflectance data shown in Figure 1.

In this paper we present and compare some simple, new algorithms for classification and whole-pixel material detection using atmospherically corrected data. These include the SAM, an extension of the SAM that accounts for the different spectral shapes of sunlight and skylight, and algorithms that use a Euclidean distance rather than a spectral angle difference metric. The most effective algorithm in this study computes the distance between the pixel spectrum and a best-fit combination of direct-sun-illuminated and sky-illuminated apparent reflectance spectra of the desired material or endmember. Another, simpler algorithm computes an analogous distance using the SAM's assumption of an invariant spectral shape. As an initial demonstration the algorithms are applied to an atmospherically corrected HYDICE (Basedow et al., 1995) image from the Forest Radiance I set studied by Healey and Slater and to a HYDICE image of the DOE ARM (Atmospheric Radiation Measurement) Site in Lamont, Oklahoma.

[1] Spectral Sciences, Inc., Burlington, MA (sag@spectral.com)
[2] Air Force Research Laboratory, Space Vehicles Directorate, Hanscom AFB, MA

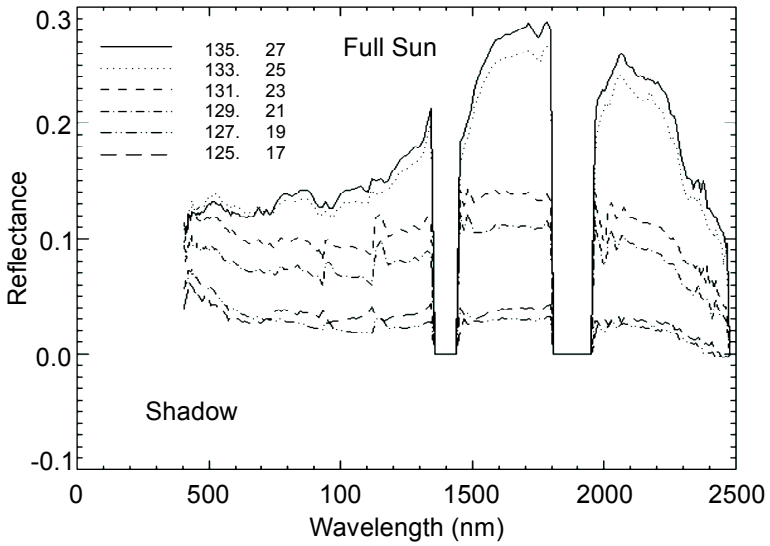

Figure 1. Apparent reflectance spectra of gravel road pixels across the edge of a tree line cast shadow (curve labels are pixel x,y coordinates). Data are from Run 7 of the HYDICE Forest Radiance I experiment. Atmospheric correction includes adjacency effect compensation. Note the relative emphasis of the short wavelengths as the shadowing increases.

2. DESCRIPTION OF APPROACH

The basic procedure involves atmospherically correcting the data to generate apparent surface spectral reflectance, calculating a skylit-to-fully-illuminated spectral ratio, applying the ratio to a fully illuminated reflectance spectrum of a chosen material to simulate its spectrum in shadow, and finally incorporating both the original and the shadowed spectrum in a detection or classification algorithm. The details are described below.

2.1 Atmospheric Correction Method

The standard equation for spectral radiance L* measured above the surface may be written as (Matthew *et al*., 2000)

$$L^* = (A\rho + B\rho_e)/(1 - \rho_e S) + L^*_a \qquad (1)$$

for ultraviolet through near-infrared wavelengths, where thermal emission is negligible. Here ρ is the pixel surface reflectance, ρ_e is a spatially convolved surface reflectance for a region surrounding the pixel, S is the spherical albedo of the atmosphere, L^*_a is the radiance backscattered by the atmosphere, and A and B are coefficients that depend on atmospheric and geometric conditions. All of these quantities are spectrally dependent. The A term in Equation (1) represents radiance from the surface that travels directly into the sensor, while the B term represents radiance from the surface that is scattered by the atmosphere into the sensor. The distinction between ρ and ρ_e accounts for the adjacency effect.

Using calculations from a radiation transport model (for example, MODTRAN (Berk *et al*., 1989)), the values of A, B, S and L^*_a can be determined and combined with a suitable point-spread function (kernel) for the ρ_e spatial convolution to iteratively solve Equation (1) for ρ. A simple method for extracting A, B, S and L^*_a from MODTRAN calculations with surface reflectances of 0, 0.5, and 1 has been described by Adler-Golden *et al*. (1999). To account for variations in the atmospheric water vapor column over the scene, a separate set of parameters is tabulated for each of a series of water amounts spanning the scene. The water amount for each pixel is retrieved using shape information from one or more water absorption bands, and the result is used to interpolate among the tabulated parameters.

2.2 Effect of Reduced Direct Solar Illumination

Equation (1) assumes full sun and sky illumination. We now consider the case where the direct sun is partially or fully blocked but the sky illumination remains. Denoting α as the fractional direct sun, Equation (1) becomes

$$L^* = (A\rho + B\rho_e)/(1 - \rho_e S) + L^*_a - (1 - \alpha)D\rho \quad (2)$$

Here $D\rho$ is the radiation that would travel along the L-shaped path from the sun to the surface to the sensor without scattering (the "direct reflected" radiance in MODTRAN).

Equations (1) and (2) together allow one to calculate the apparent reflectance spectrum ρ_p of a partially sunlit surface that is returned by a standard atmospheric correction algorithm that assumes full illumination. To do this, we replace ρ with ρ_p in Equation (1) and equate the spectral radiance to that of Equation (2). This leads to the following relationship between the two reflectance spectra:

$$\rho_p = \rho[1 - (1 - \alpha)D(1 - S\rho_e)/A] \quad (3)$$

According to Equation (3), the observed spectrum ρ_p can be written as a linear combination of a shadow spectrum ($\alpha = 0$), given by $\rho[1 - D(1 - S\rho_e)/A]$, and either the ordinary full-illumination spectrum ρ or the spectrum $\rho D(1 - S\rho_e)/A$ that is attributable to direct sun illumination only (no skylight). The quantity $R = 1 - D(1 - S\rho_e)/A$ is the spectral ratio between the shadowed spectrum and the fully illuminated spectrum, and depends only on quantities that are calculated during the atmospheric correction process.

In strict terms, R is not constant over the scene because of variation in the spatially convolved reflectance ρ_e. However, in most situations this variation can be neglected. At the shortest visible wavelengths, where S is largest, the atmospheric scattering is dominated by Rayleigh scattering, for which the range of the convolution kernel is typically of order 1 km. With a kernel of this size, ρ_e tends to vary little over the scene as long as the different surfaces types are reasonably well distributed spatially. At longer wavelengths the kernel range is shorter, but here $S << 1$ for typical aerosol loadings, so that any ρ_e variation will have only a small effect. Therefore, to a good approximation, we may replace ρ_e with the scene-average reflectance ρ_a. This results in a simple expression for the shadow (full sky-illuminated) to full illumination spectral ratio,

$$R = 1 - D(1 - S\rho_a)/A \quad (4)$$

that is independent of both location in the scene and the spectral properties of the surface. R is of course dependent on the atmospheric properties, particularly the aerosol amount and type, as well as the solar and viewing geometries.

A typical calculation of R using MODTRAN appears in Figure 2. Since the Equation (4) result is close to the simpler expression 1-D/A that neglects $S\rho_a$, the replacement of ρ_e with the scene-average ρ_a should be a negligible source of error. The absorption band structure in R, which is mainly from water vapor, arises because the skylight takes a somewhat longer average path through the atmosphere than the direct sun. With typical atmospheric correction codes, this structure tends not to appear in shadows because the code adjusts the retrieved water amount to compensate. To account for this adjustment, R may be computed using slightly different water amounts in D and A so as to minimize the band structure.

2.3 Shadow-Invariant Detection and Classification

A variety of hyperspectral algorithms exist for the detection of desired materials at the sub-pixel or whole-pixel levels. Unconstrained subspace projection (Chang *et al*., 1998), constrained unmixing (Keshava *et al*., 2000), and the matched filter (MF) and Constrained Energy Minimization (CEM) (Farrand and Harsanyi, 1997) algorithms are suitable for sub-pixel detection. Classification algorithms, which assign each pixel to an "endmember" spectrum, work well for whole-pixel detection if the desired material is taken as an endmember. The simplest of these algorithms, which require definitions of endmember spectra but not their statistics, use either Euclidean distance or spectral angle as a spectrum difference metric. The spectrum is assigned to the endmember that gives the minimum distance or angle, or equivalently the maximum angle cosine.

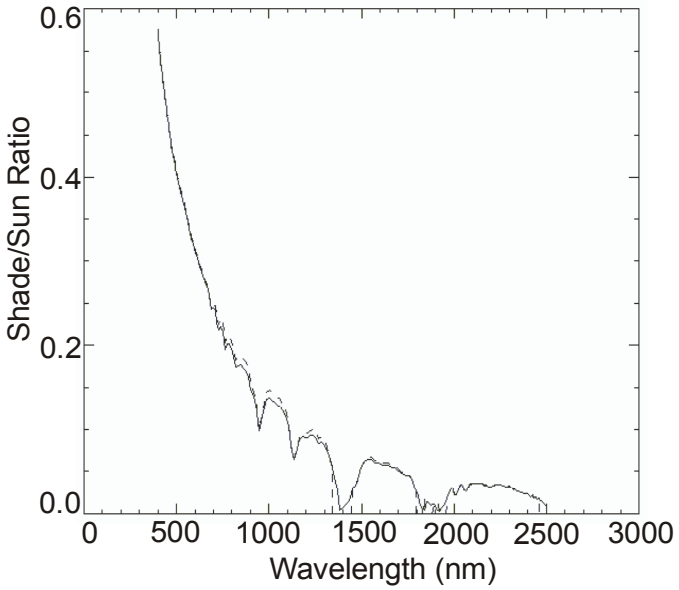

Figure 2. MODTRAN-calculated shadow to full illumination reflectance ratio for the HYDICE Forest Radiance Run 7 scene (56^o solar zenith angle, 25 km urban haze, 2200 atm-cm water vapor). Solid line is 1-D/A; dashed line is from Equation (4).

One can envision generalizing the above methods to accommodate the sky-versus-sun spectral difference by representing the desired or endmember material spectrum as some linear combination of the skylit spectrum and the direct sun-illuminated spectrum (the fully illuminated spectrum minus the skylit spectrum). Examples of generalized classification algorithms are given below. *If the sky is considered as a spectrally uniform source, then all combinations of sky and sun illumination can be represented by some positive linear combination of those two spectra,* even when there is less than full sky illumination. As a special case, if one imposes a full-sky illumination constraint the linear combination is defined simply by the direct-sun fraction α.

2.3.1 Algorithms Based on Spectral Angle

The SAM computes the spectral angle between the unknown pixel spectrum and the endmember (or desired) spectrum, a quantity that is amplitude independent. The angle cosine is given by

$$p = \boldsymbol{r}_i^T \boldsymbol{d} \,/\, |\boldsymbol{r}_i||\boldsymbol{d}| \tag{5}$$

where $\boldsymbol{r}_i^T$ is the pixel spectrum, $\boldsymbol{d}$ is the endmember (or desired) spectrum; bold font is used to denote vector quantities and operations.

We may write a generalization of the SAM that explicitly accounts for the spectral variation caused by reduced direct sun:

$$p_{\mathrm{L}} = \boldsymbol{r}_i^T \boldsymbol{d}_p \,/\, |\boldsymbol{r}_i||\boldsymbol{d}_p| \tag{6}$$

Here $\boldsymbol{d}_p$ is the least-squares best-fit linear combination of direct sun-illuminated and sky-illuminated endmember reflectance spectra for each pixel and p_{L} is the cosine of the spectral angle between the pixel spectrum and $\boldsymbol{d}_p$. If we assume full sky illumination, $\boldsymbol{d}_p$ is written as

$$\boldsymbol{d}_p = \alpha \boldsymbol{d}_1 + \boldsymbol{d}_2 \tag{7}$$

where $\boldsymbol{d}_2$ is the spectrum of the endmember in shadow (*i.e.*, $\boldsymbol{d}$ scaled by R) and $\boldsymbol{d}_1$ is the direct-sun spectrum $\boldsymbol{d} - \boldsymbol{d}_2$. The best-fit direct sun fraction α for the pixel is given by

$$\alpha = (\boldsymbol{r}_i - \boldsymbol{d}_2)^T \boldsymbol{d}_1 / (\boldsymbol{d}_1^T \boldsymbol{d}_1) \tag{8}$$

To keep α physically meaningful it should be restricted to values between 0 and 1. This enhanced version of the SAM is referred to in this paper as *SAM-IM*, for *Spectral Angle Mapper with Illumination Matching*.

2.3.2 Algorithms Based on Distance

The simplest distance metric for detection or classification is the Euclidean distance between the desired or endmember spectrum and the unknown pixel spectrum,

$$D = |\boldsymbol{r}_i - \boldsymbol{d}| \tag{9}$$

A corresponding distance may be defined in which the endmember illumination is best fit to the pixel spectrum:

$$D_{\mathrm{L}} = |\boldsymbol{r}_i - \boldsymbol{d}_p| \tag{10}$$

We have found that the full-sky constraint used to define $\boldsymbol{d}_p$ in Equation (7) is very limiting with the distance metric, since it does not allow brightness matching when the shadows are only partially illuminated by the sky. To overcome this problem $\boldsymbol{d}_p$ is redefined by including β as an effective sky illumination fraction:

$$\boldsymbol{d}_p = \alpha \boldsymbol{d}_1 + \beta \boldsymbol{d}_2 \tag{11}$$

α and β are determined from a least-squares fit to the pixel spectrum. The unconstrained solutions, obtained by 2-dimensional projection, are

$$\alpha = (\boldsymbol{r}_i^T \boldsymbol{u}_1 - w \boldsymbol{r}_i^T \boldsymbol{u}_2) / |\boldsymbol{d}_1|(1 - w^2) \tag{12a}$$

$$\beta = (\boldsymbol{r}_i^T \boldsymbol{u}_2 - w \boldsymbol{r}_i^T \boldsymbol{u}_1) / |\boldsymbol{d}_2|(1 - w^2) \tag{13b}$$

where $\boldsymbol{u}_1$ and $\boldsymbol{u}_2$ are the unit vectors $\boldsymbol{d}_1/|\boldsymbol{d}_1|$ and $\boldsymbol{d}_2/|\boldsymbol{d}_2|$, respectively, and $w = \boldsymbol{u}_1^T \boldsymbol{u}_2$. If either α or β lie outside the physically plausible 0 to 1 interval, the results are replaced with a constrained solution, which is omitted here for brevity. The classification algorithm based on Equations (10)-(13b) is referred to in this paper as *MD-IM*, for *Minimum Distance with Illumination Matching*.

An alternative, simpler distance metric can be generated by assuming that the spectral shape is illumination-independent, as in the SAM. This leads to a definition of $\boldsymbol{d}_p$ as the projection of the pixel spectrum onto the fully illuminated endmember material,

$$\boldsymbol{d}_p = \boldsymbol{u}\, \boldsymbol{r}_i^T \boldsymbol{u} \tag{14}$$

where $\boldsymbol{u}$ is the endmember unit vector $\boldsymbol{d}/|\boldsymbol{d}|$. The projection magnitude $\boldsymbol{r}_i^T \boldsymbol{u}$ can be limited to a maximum of $|\boldsymbol{d}|$, the length of the endmember, to insure that the illumination does not exceed that of the full sun and sky. This constraint effectively prevents the pixel from being classified with a dimmer endmember, as can happen with the SAM and SAM-IM. We refer to the classification algorithm based on Equations (10) and (14) as *PD*, for *Projection Distance*. While not as accurate as the MD-IM algorithm, a practical advantage is that no information on the shadow-to-full-illumination reflectance ratio is required, making it suitable with atmospheric correction methods such as the ELM that do not use radiation transport calculations.

3. ILLUSTRATIONS

3.1 Shadowed Material Detection

To test the effectiveness of the SAM in cast shadows and assess the importance of the different spectral shapes of sunlight and skylight, the SAM and SAM-IM algorithms were exercised on an early morning image, Run 7, from the 1995 HYDICE Forest Radiance I data. Figure 3 shows a portion of the image where an L-shaped loop

of gravel road (dotted line) runs along a tree line. The short side of the L is in the open but is shadowed by the tree line to the left. The long side of the L is both shaded and partly obscured by overhanging trees. On the opposite side of the road is a line of test objects. The purpose of the demonstration was to find all non-obscured gravel road pixels, including the parts of the road in shadow, using spectral information only (i.e., no spatial filtering). This detection problem is a fairly challenging one, because the actual road spectrum varies over the scene and also because it lacks obvious unique spectral features.

The hyperspectral image was atmospherically corrected using the code developed by Matthew *et al*. (2000), which is based on MODTRAN4 (Berk *et al*., 1998) and includes an adjacency effect compensation and aerosol retrieval capability. The code was modified to output the D coefficient in Equation (2). A visible range of around 25 km was retrieved with the urban aerosol model. For simplicity we assumed that the sunlit road could be represented by the spectrum from a single pixel. The SAM and SAM-IM angle cosine outputs were calculated and used as the road detection metric; a pixel was identified as road if a threshold was exceeded.

Figure 3. Forest Radiance I Run 7 scene. The right hand image shows the location of a gravel road at the tree line.

The results are summarized in Figure 4, which depicts the output amplitudes as gray scale images in the left-hand column (white = maximum) and the results after thresholding in the right-hand column. In the top two images, the sunlit road spectrum is input, and the SAM yields a strong response to the sunlit road pixels but a very poor response to the shadowed road pixels. In the middle four images, a shadowed road spectrum is input. Here the SAM responds well to the shadowed road and almost as well to shadows cast on the field by the tree line and the test objects, but the response to the sunlit road is poor. Nearly identical results are obtained using an actual shadowed road spectrum (second row) and a spectrum simulated from the sunlit spectrum and the spectral ratio R (third row).

As shown in the bottom two images in Figure 4, the SAM-IM essentially combines the detection capabilities of the sunlit and the shadowed SAM runs. Compared to the ordinary SAM there is some sacrifice in the ability to reject false positives, which, as seen from Figure 3, are mainly from shadows and dead grass. However, this is more than compensated by the new capability to detect the road in shadow.

3.2 Shadow-Invariant Classification

As a second demonstration, we compare the angle metrics of the SAM and SAM-IM with the distance metrics of the PD and MD-IM algorithms for surface classification. The algorithms were applied to an image of the Lamont, Oklahoma DOE ARM site taken by HYDICE in June 1997 (Figure 5) with a very low sun angle (around 15^{o} elevation), resulting in long shadows cast by trees and buildings. The image was atmospherically corrected, and seven representative spectra were manually selected as endmembers. The spectra are grass, dirt (from the furrowed field at the lower left), building roof (from one of the brighter building pixels), pond, black panel (the nominal 3% reflective panel at the upper right corner of the array), road, and driveway (a pixel in the open area between the buildings). These spectra all have distinct shapes, except for the road and driveway, which differ somewhat in brightness but otherwise are very similar. The distinction between the road and driveway classes turns out not to be meaningful, so these classes have been lumped together in the presentation of results.

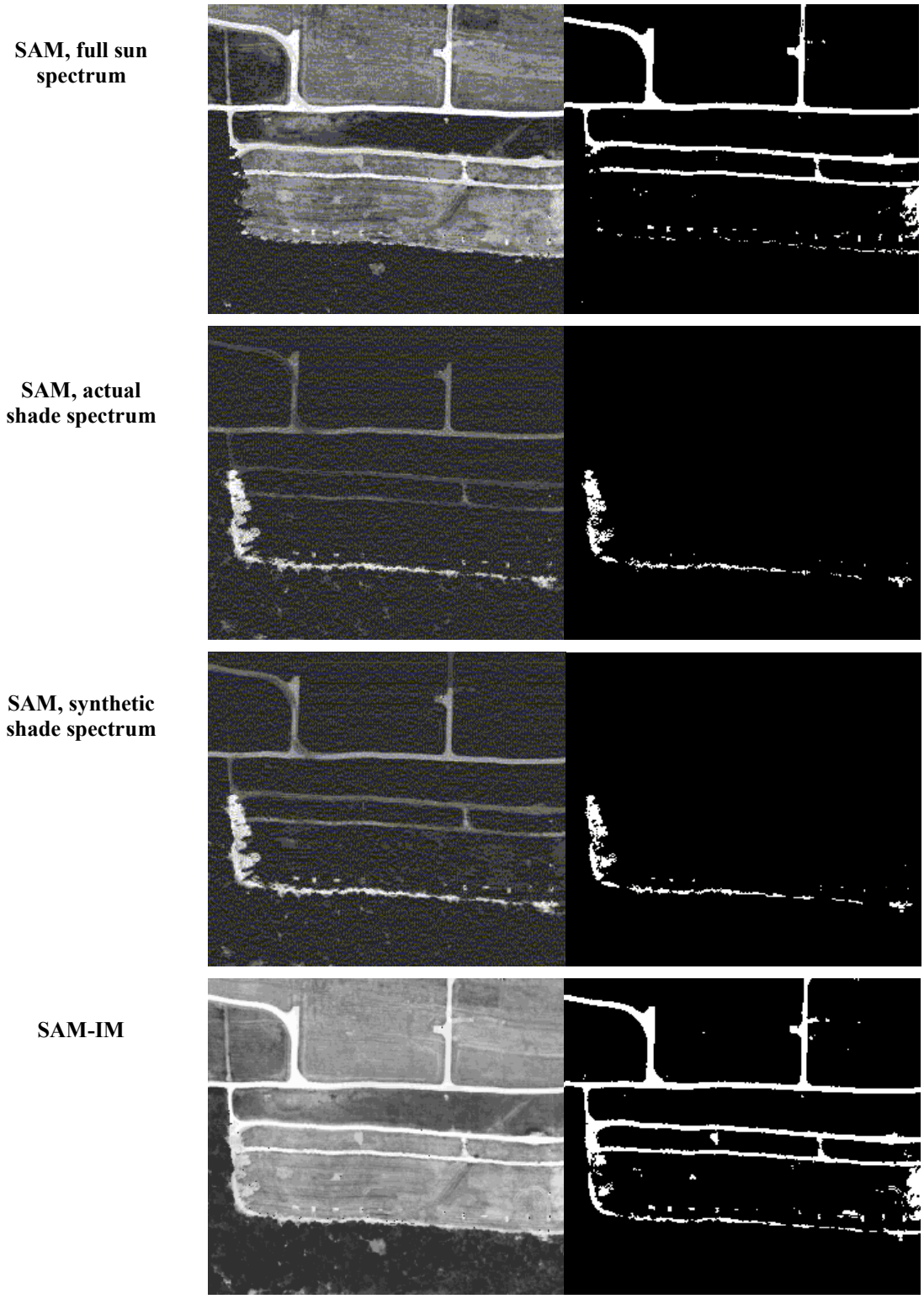

Figure 4. Road detection results. Left-hand images are the angle cosine outputs; right-hand images are the results after thresholding.

The classification results are shown in Figures 6a-d. Enlargements of Figures 5 and 6a-d that focus on the main cluster of buildings appear in Figures 7 and 8a-d. The color scheme in the classification maps is green = grass, ochre = dirt, pink = roof, dark blue = pond, black = panel, gray-blue = road/driveway.

Figure 5. HYDICE ARM Site scene, Run 22.

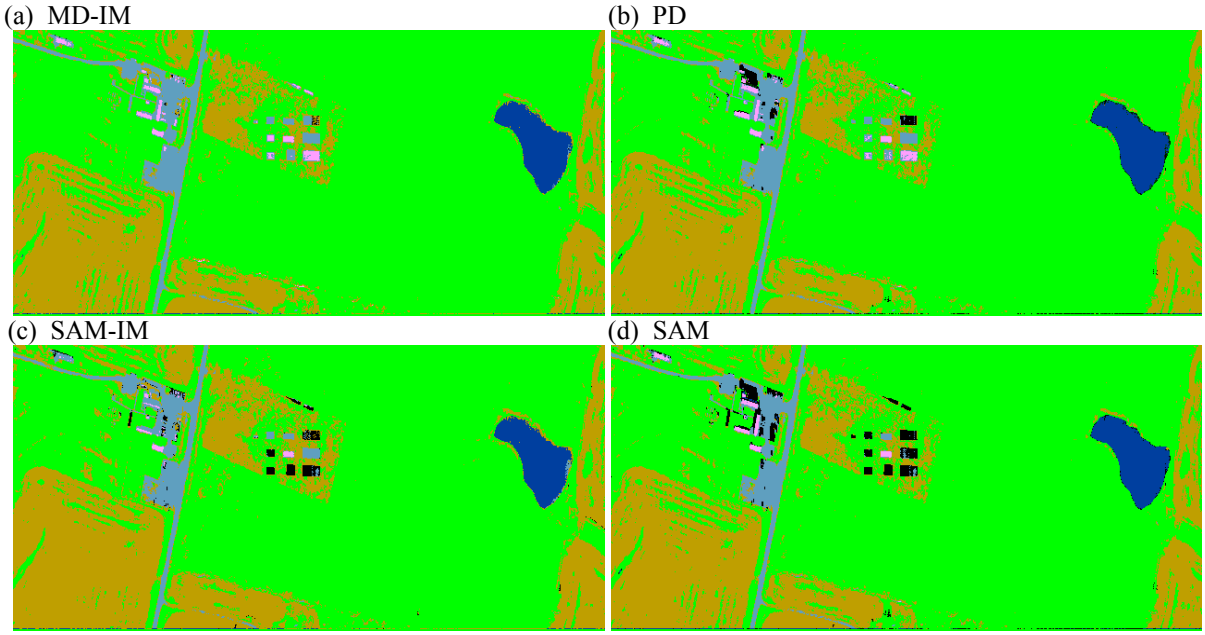

Figure 6a-d. ARM site classification maps.

The main differences among the classifications revolve around the black panel, road/driveway and building classes. The algorithms that do not include the blue-skewing effect of the sky (PD and SAM) classify the shadows on the road/driveway with the black panel, while those that include the skewing correctly assign nearly all of them to the road/driveway class. On the other hand, shadows on the grass are correctly classified as grass by all of the algorithms, including the SAM. The building pixels are classified well by all algorithms except the SAM-IM, which mis-classifies the building roofs that face away from the sun.

The two spectral angle-based algorithms assign a large number of the calibration panels to the black panel class, even those that are much brighter than the black panel. In contrast, the distance-based algorithms assign only portions of the two darkest panels to the black panel class. These results are consistent with the discussion in Section 2.3.2. The MD-IM black panel class is actually a bit too restricted; many of the black panel pixels are assigned to the soil class, apparently because the difference in brightness and color can together be compensated by reduced illumination.

The MD-IM algorithm was also run with different constraints on the sky fractional illumination β. With a lower limit of 0.5 most shadows were properly classified. However, raising the limit to 1.0 gave very poor results; even shadowed grass was mis-classified. The problem may be that the skylight is very anisotropic, increasing strongly near the sun especially when it is low; thus, even a small obscuration of the sky around the sun can reduce the illumination to well below the full sky total. The SAM-IM algorithm performs better than the MD-IM with $\beta = 1$ because the spectral angle is insensitive to the illumination intensity.

Figure 7. Enlargement of Figure 5.

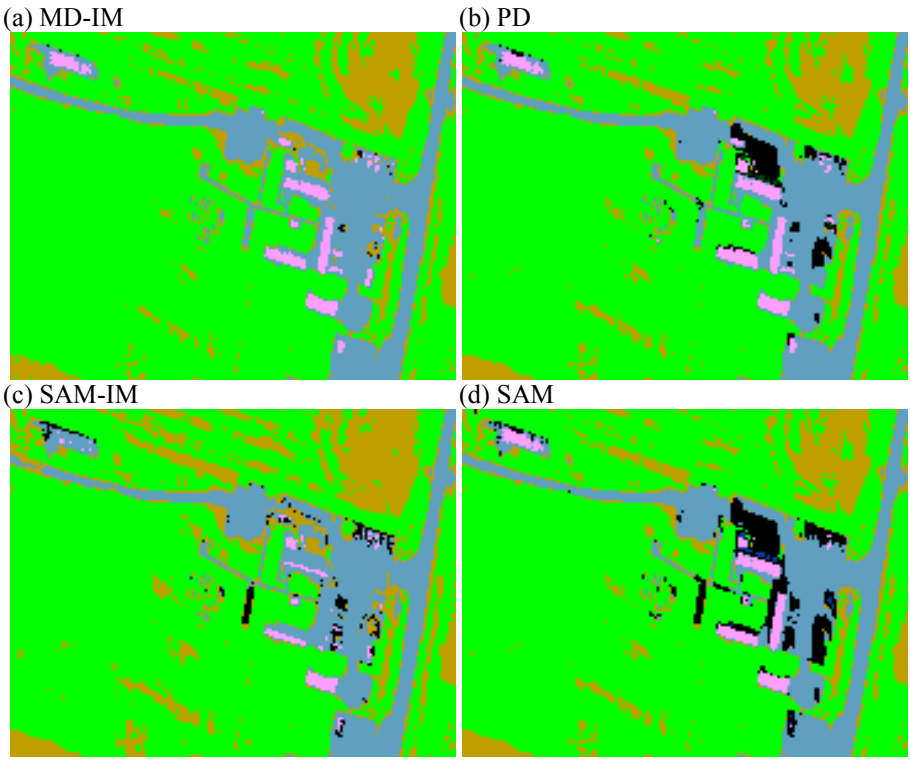

Figures 8a-d. Enlargements of Figures 2a-d.

4. CONCLUSIONS

Starting from radiation transport equations and spectral angle or Euclidean distance metrics, some simple algorithms for illumination-invariant detection or classification of surface materials in atmospherically corrected hyperspectral images have been formulated. In initial demonstrations on HYDICE data the new algorithms performed significantly better in shadow than the Spectral Angle Mapper (SAM). The most successful algorithm, MD-IM, uses a constrained 2-dimensional projection of the pixel spectrum onto apparent endmember reflectance spectra that correspond to illumination by direct sun and by the sky. The sky-illuminated spectrum is simulated from the ordinary reflectance spectrum using a spectral ratio calculated from the MODTRAN radiation transport model. Another algorithm, PD, does not use this ratio but still outperformed the SAM in our tests. Both the PD and MD-IM algorithms generate a spectral distance metric that incorporates a maximum illumination constraint. The SAM has no such constraint, and thus can assign a pixel to the class of a dimmer endmember, which is not physically justifiable for horizontal Lambertian surfaces. For situations where such an assignment may be sensible (for example, when the target brightness is inherently variable due to specular behavior and varying orientation), the allowable maximum illumination could be increased. The sky illumination in the MD-IM algorithm can be constrained with a lower bound; however, the current study did not find this to be helpful.

Further work is needed to evaluate of the performance of the new algorithms and metrics on a broader range of data and to compare the results with the radiance simulation approach of Healey and Slater (1999). We anticipate that the best performance may be attainable with algorithms, such as the MD-IM, that use a low-dimensional projection, incorporate physical constraints, and take advantage of state-of-the-art radiation transport codes and processing algorithms that remove sensor-related artifacts (Boardman, 1998). In addition to detection and classification, the PD and MD-IM distance metrics may prove valuable in clustering or other methods for endmember selection. Finally, we note that with either an atmospheric correction or simulation-based approach, inclusion of the adjacency effect is essential for the accurate treatment of dark surfaces and shadows (see Figure 5 of Adler-Golden et al. (1999)).

5. ACKNOWLEDGEMENTS

The authors greatly thank the US Air Force for support under Contract Nos. F19628-99-C-0031 and F19628-00-C-0022 and the Spectral Information Technical Application Center (Fairfax, VA) for providing the HYDICE data.

References

Adler-Golden, S. M., M.W. Matthew, L. S. Bernstein, R. Y. Levine, A. Berk, S. C. Richtsmeier, P. K. Acharya, G. P. Anderson, G. Felde, J. Gardner, M. Hoke, L. S. Jeong, B. Pukall, A. Ratkowski and H.-H Burke, 1999, "Atmospheric Correction for Short-wave Spectral Imagery Based on MODTRAN4," *SPIE Proc. Imaging Spectrometry V*, **3753,** pp. 61-69.

Basedow, R.W., D.C. Armer, and M.E. Anderson, 1995, "HYDICE System: Implementation and Performance," *SPIE Proc. Imaging Spectrometry V*, **2480**, pp. 258-267.

Berk, A., L. S. Bernstein, G. P. Anderson, P. K. Acharya, D. C. Robertson, J .H. Chetwynd and S. M. Adler-Golden, 1998, "MODTRAN Cloud and Multiple Scattering Upgrades with Application to AVIRIS," *Remote Sens. Environ.*, Vol. **65**, pp. 367-375.

Berk, A., L. S. Bernstein and D. C. Robertson, 1989, "MODTRAN: a moderate resolution model for LOWTRAN7," *GL-TR-89-0122*, Air Force Geophys. Lab., Hanscom AFB, MA, 38 pp.

Boardman, J.W., 1998, "Post-ATREM Polishing of AVIRIS Apparent Reflectance Data using EFFORT: a Lesson in Accuracy versus Precision," *Summaries of the Seventh JPL Airborne Earth Science Workshop,* JPL Publication 97-21, Vol. 1, p. 53.

Chang, C-I., Xiao-Li Zhao, M. L. G. Althouse and J. J. Pan, "Lease Squares Subspace Projection Approach to Mixed Pixel Classification for Hyperspectral Images," *IEEE Trans. on Geosci. Remote Sensing*, Vol. **36**, No. 3, (1998).

Farrand, W. H. and J.C. Harsanyi, 1997, "Mapping the Distribution of Mine Tailings in the Coeur d'Alene River Valley, Idaho, Through the Use of a Constrained Energy Minimization Technique," *Remote Sens. Environ*., Vol. **59**, pp. 64-76.

Gao, B. -C., K. B. Heidebrecht, and A. F. H. Goetz, 1996, "Atmospheric Removal Program (ATREM) Version 2.0 Users Guide," Center for the Study of Earth from Space/CIRES, University of Colorado, Boulder.

Green, R. O., D. A. Roberts, and J. E. Conel, 1996, "Characterization and Compensation of the Atmosphere for Inversion of AVIRIS Calibrated Radiance to Apparent Surface Reflectance," *Summaries of the 6th Annual JPL Earth Science Workshop*, *JPL Publication 96-4*, Vol. **1**, pp. 135-146.

Healey, G. and D. Slater, "Models and Methods for Automated Material Identification in Hyperspectral Imagery Acquired Under Unknown Illumination and Atmospheric Conditions," *IEE Trans. Geosci. Remote Sensing*, Vol. **37**, pp. 2706-2717 (1999).

Keshava, N., J. Kerekes, D. Manolakis, and G. Shaw, 2000, "An Algorithm Taxonomy for Hyperspectral Un-mixing," *SPIE Proc. Algorithms for Multispectral, Hyperspectral, & Ultraspectral Imagery VI*, **4049**, pp. 42-63.

Kruse, F.A. *et al*., 1993, "The Spectral Image Processing System (SIPS)--Interactive Visualization and Analysis of Imaging Spectrometer Data," *Remote Sens. Environ*., Vol. **44**, pp. 145-163.

Matthew, M.W., S.M. Adler-Golden, A. Berk, S.C. Richtsmeier, R.Y. Levine, L.S. Bernstein, P.K. Acharya, G.P. Anderson, G.W. Felde, M.P. Hoke, A. Ratkowski, H.-H. Burke, R.D. Kaiser, and D.P. Miller, 2000, "Status of Atmospheric Correction Using a MODTRAN4-based Algorithm," *SPIE Proceeding, Algorithms for Multispectral, Hyperspectral, and Ultraspectral Imagery VI*, **4049**, pp. 199-207.

Richter, R., 1996, "Atmospheric Correction of DAIS Hyperspectral Image Data," *SPIE Proc. Algorithms for Multispectral and Hyperspectral Imagery II,* **2758**, pp. 390-399.